ORIGINAL ARTICLE

CrossMark

Focal mechanism determination for microseismic events and its application to the left bank slope of the Baihetan hydropower station in China

Feng Dai[1] · Peng Jiang[1] · Nuwen Xu[1,2] · Wenfu Chen[3] · Yaosheng Tan[3]

Abstract

Determination of the focal mechanism of microseismic (MS) events occurring in rock engineering plays an important role in hazard evaluation and forecasting. A complete moment tensor inversion strategy is proposed to analyse MS events recorded at the left bank slope of the Baihetan hydropower station, southwest of China. A coordinate system rotation procedure is adopted to construct a reliable 1-D velocity model for the Green's function calculation. The layered velocities are accurately determined by inversion using the recorded blasts and geological survey results. To reduce the influence of noise contamination, only the waveforms in the frequency range of 60–150 Hz are analysed. Before moment tensor inversion, a relocation procedure using an eikonal solver is performed to accurately locate seismic sources. A robust global optimization routine is applied to maximize the objective function, thereby determining the focal mechanism. The proposed method is tested using a hypothetical seismic source in the sensor network used for monitoring MS events in the rock slope. The synthetic test shows that the method is robust and can provide accurate solutions when subject to location error, noise contamination and velocity model disturbances. The analysis results of the 12 MS events show that the moment tensors characterizing MS events present significant non-double-couple components and that the majority of the MS events have a strike orientation in accordance with that of the main staggered zones.

Keywords Focal mechanism · Rock slope · Microseismic events · Waveform matching · Non-double-couple components

Introduction

Rock engineering activities such as blasting excavation and hydrofracturing inevitably produce changes in rock mass structures and in situ stress re-distribution, which may induce microcracks in the rock mass. The occurrence and development of microcracks emit elastic waves, namely microseismic (MS) events. As an effective monitoring method for rock damage, MS monitoring can continuously detect the time, location and intensity of microfractures occurring in the rock mass and, thus, can provide references for engineering stability assessment and hazard forecasting (e.g., Köhn et al. 2016; Liu et al. 2013; Lu et al. 2015; Tang and Xia 2010; Xu et al. 2011, 2014, 2015, 2016a, b).

In addition to the time, location and intensity, derivation of the source-focal mechanism is also important for MS events. In seismology, most earthquakes are induced by shear slip along a pre-existing fault and display a double-couple mechanism. Thus, earthquakes studies have commonly assumed the source to be double-couple mechanism (Li et al. 2011; Zhang et al. 2014). In sharp contrast to earthquakes, MS events can be induced by non-shear processes. Recent studies have shown the existence of non-double-couple components for MS events in hydrofracturing (Šílený et al. 2009; Song and Toksöz 2011) and underground caverns (Kühn and Vavryčuk 2013; Šílený and Milev 2006; Xiao et al. 2016). On the other hand, the double-couple assumption can also

✉ Nuwen Xu
  xunuwen@scu.edu.cn

1 State Key Laboratory of Hydraulics and Mountain River Engineering, College of Water Resource and Hydropower, Sichuan University, Chengdu 610065, Sichuan, People's Republic of China

2 State Key Laboratory of Geo-Hazard Prevention and Geo-Environment Protection, Chengdu University of Technology, Chengdu 610059, Sichuan, People's Republic of China

3 China Three Gorges Projects Development Co., Ltd, Beijing 100038, People's Republic of China

distort the moment tensor and bias the fault-plane solution (Vavryčuk 2007). Therefore, a detailed investigation on the complete moment tensor is crucial not only for revealing the non-double-couple components of MS events but also for obtaining the correct fault-plane solutions.

The moment tensor has been widely used to reveal the mechanism of MS events. Šílený et al. (2009) used the moment tensor to investigate the source mechanisms of seismicity induced by hydraulic fracturing. They found significant non-double-couple source mechanisms with a positive volumetric component. Song and Toksöz (2011) derived the moment tensor for seven selected testing events using data from a single monitoring well during hydraulic fracturing. Their results suggested that most of the events displayed a dominant double-couple component. Kühn and Vavryčuk (2013) determined the full moment tensor of five blasting events and MS events recorded in a very heterogeneous mine. They indicated that the blast events were characterized by dominant positive isotropic components and that the MS events were characterized by significant negative isotropic and compensated linear vector dipole components. In rock slope engineering, especially concerning high stratified rock slopes, the failure modes are rather complicated. For example, the bedding rock strata are prone to slide and cause MS events with high double-couple components. On the other hand, the excavation of the tunnels in the rock slope may cause collapses due to the relatively weak strength of discontinuities and bring about MS events with significant non-double-couple components. The focal mechanism of MS events detected by the MS monitoring system is of significance for the stability analyses of rock slopes, as well as their potential risk forecasting. The moment tensor can serve as a detection tool to determine the double-couple and non-double-couple components and thus help to understand the physics of fracture processes. However, few reports can be found in the study of focal mechanism of microfractures using the moment tensor of MS events recorded in rock slopes.

An accurate determination of the full moment tensors of MS events is an involved and data-intensive task. The moment tensor inversion procedure is sensitive to the velocity model and the source location. Hence, determining how to establish an accurate velocity model and retrieve a reliable source position is crucial to the inversion process. Moreover, the method adopted to find out the optimum moment tensor solution is also important to the robustness of the moment tensor inversion procedure. Using the waveform matching method, this study attempts to retrieve the moment tensor solution of the MS events that occurred in the left bank slope of the Baihetan hydropower station, southwest China. To establish an accurate layered velocity model, a rotation procedure is adopted according to the attitude of rock strata, and the wave speeds are determined by inversion based on

geological survey results and recorded blasts. After adopting the derived layered velocity model, an accurate relocation procedure is performed to reduce the source location error. Finally, a global optimization algorithm is used to accelerate the search procedure, thereby finding the best match between the modelled waveforms and the observed waveforms. The proposed method is validated with a synthetic event and then applied to the selected MS data recorded in the left bank slope at the Baihetan hydropower station.

Project overview

Engineering background

The Baihetan hydropower station is located at the downstream of the Jinsha River in Southwest China (Fig. 1). This station is a giant hydropower station with a 289-m-high double-curvature arch dam and a total installed capacity of 16,000 MW. Figure 2 shows the left bank slope after excavation. The slope region is characterized by canyon geomorphology, with a 200–440 m height below the plateau. The strata in the station region mainly belong to the Emeishan basalts ($P_2\beta$) and can be divided into 11 layers ($P_2\beta_1$–$P_2\beta_{11}$) according to the lava eruption episodes. The strata outcropped in the slope mainly belongs to the 2th–4th layers ($P_2\beta_2$–$P_2\beta_4$) and are characterized by bedding structures, as shown in Fig. 2. According to the geological investigation during excavation, the main features of the geologic structures in the rock slope are the primary and faulted structures, and the attitude of the rock strata is N35°–55°E, SE∠15°–20°. The C_3, C_{3-1} interlayer staggered zones and several intrastratal staggered zones, such as LS_{331}, LS_{337}, and LS_{342}, have the potential to be the sliding surfaces of the slope. Some faults, such as F_{17} and F_{110}, which intersect the staggered zones, may also form potential unstable blocks.

According to the excavation schedule, the excavation of the left bank slope started on September 22, 2013. Up to December 26, 2014, the slope was excavated to EL. 628 m (see Fig. 2). From January 2015 to February 2016, the excavation of the left bank slope was suspended due to some large deformations and failure occurring at the bottom of the rock slope. The construction was mainly concentrated on the excavation of various tunnels (i.e., drainage tunnels and grouting tunnels) in the rock slope and on the supporting and grouting of the slope.

Description of the MS monitoring system

A high-precision MS monitoring system, produced by ESG (Engineering Seismology Group), Canada, was installed in the left bank slope to monitor the microfractures induced by the excavation in real time (Dai et al. 2017). The MS
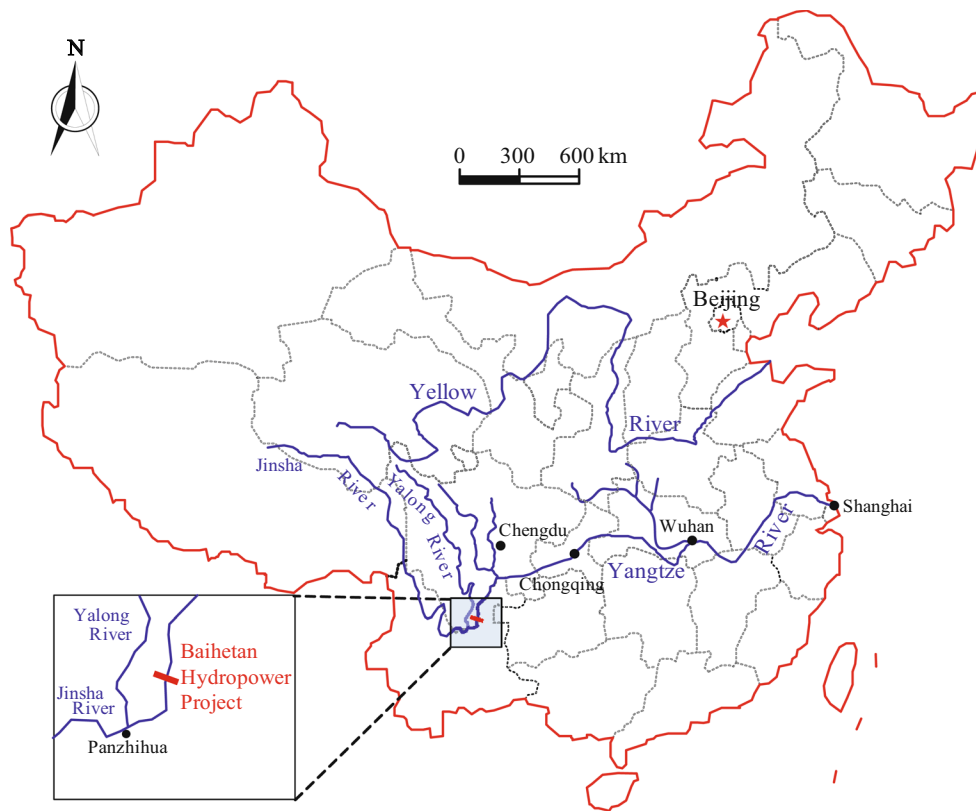
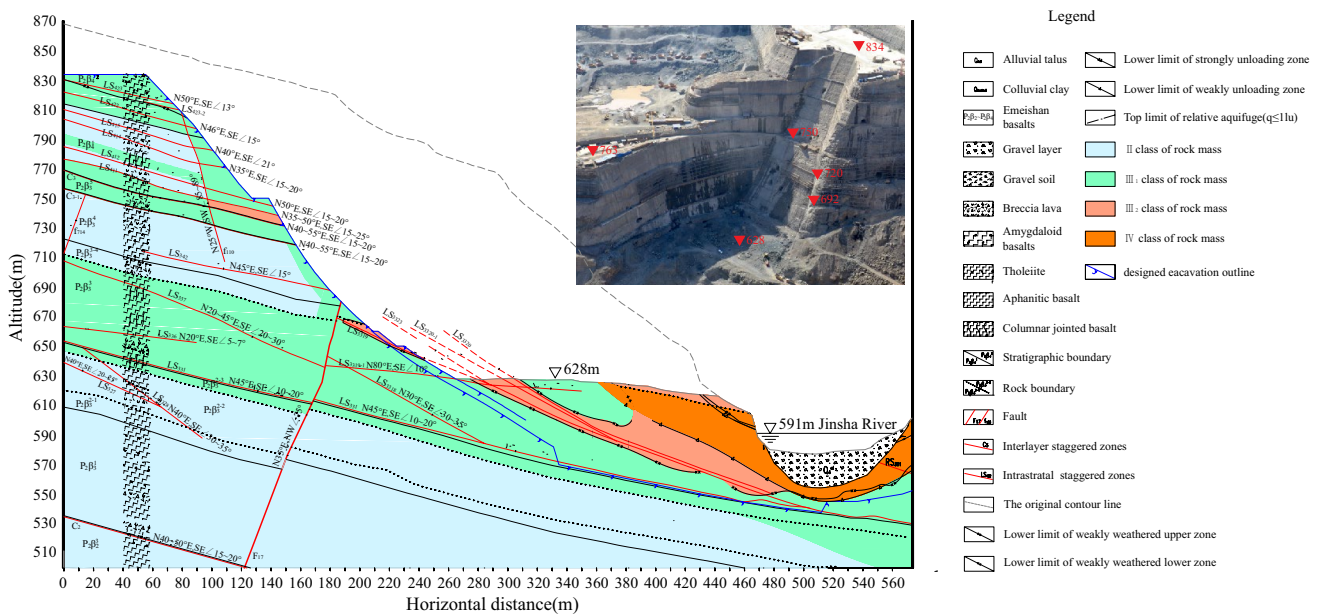**Fig. 1** Regional map of the Baihetan hydropower station

Fig. 2 Geological cross-section of the left bank slope at the Baihetan hydropower station along the dam axis, the photo of left bank slope after excavation in January 2015 is inserted

monitoring system mainly consists of a Hyperion digital signal processing system, a data acquisition system, and 18-channel sensor network (6 uniaxial geophones with a response frequency band of 5–2.5 kHz and 12 uniaxial accelerometers with a response frequency band of 20 Hz–5 kHz), as shown in Fig. 3. The 9th, 10th, and 11th channels were replaced by a triaxial accelerometer in November 2015. The sensors are cemented in boreholes drilled vertically in the sidewalls of the excavated tunnels at EL. 750 m, EL. 660 m, and EL. 610 m, as shown in Fig. 3b–d. The sensor array can cover an area of approximately 300 m (vertical direction) ×400 m (along the arch axis direction) ×400 m (normal to the arch axis direction). The 18-channel network can monitor the disturbed rock mass in real time, and the received signals are transmitted to the acquisition system via copper twisted-pair cables. The acquisition system is connected to the Hyperion digital signal processing system using optical fibre cables to ensure the stability of signals and to minimize the attenuation during propagation.

The data acquisition systems record the data at a sampling frequency of 20 kHz when the signal exceeds the given trigger threshold, defined as Short Time Average vs. Long Time Average (STA/LTA). Furthermore, a homogeneous model, in which the P- and S-wave speeds are set to be 4700 and 2714 m/s, respectively, is used to calculate the event location as well as the source parameters such as energy, moment magnitude, and source radius (Xu et al. 2014).

Methodology

Inversion of complete moment tensor

The ISOLA code (Sokos and Zahradnik 2008) is adopted to model the waveforms. The discrete wavenumber method (Bouchon 1981, 2003) is used to calculate the Green's function, defined as the earth response (Carvalho et al. 2015). The Green's function is calculated based on the infinite model or half-space model. The structure between the seismic source and the stations is simplified as a 1-D layered medium.

The source-time function is assumed to be a delta function (Sokos and Zahradnik 2008; Vavryčuk and Kühn 2012), and the actual time dependence of the source-time function is neglected. Both the monitoring data and the modelled waveforms are filtered in the frequency range of 60–150 Hz, which contains the main energy distribution of the waveforms collected in the field. The purpose of the filtering
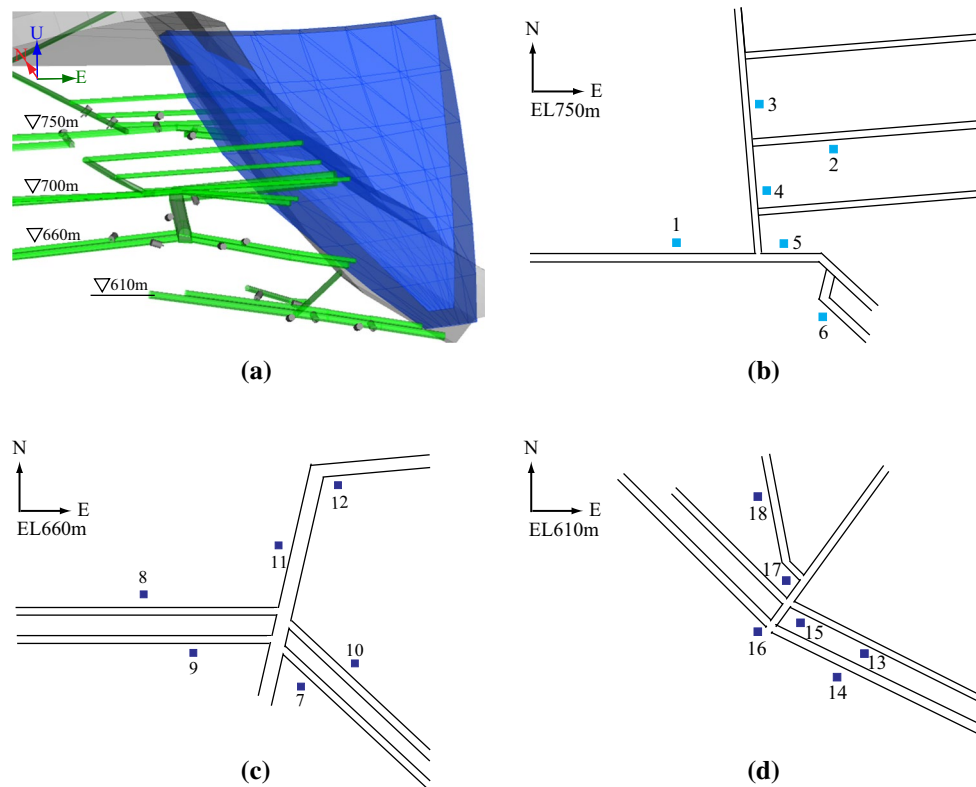

Fig. 3 Spatial distribution of the sensor network in the rock slope. **a** 3D arrangement of the sensor network, **b** the sensor layout at EL. 750 m, **c** the sensor layout at EL. 660 m, and **d** the sensor layout at EL. 610 m. Herein, the blue/green dots represent the geophones/accelerometers, respectively

process is to increase the efficiency of the inversion by removing the background noise, especially the interference of alternating current, whose frequency is 50 Hz.

To evaluate the similarity between the modelled and recorded data, the following objective function is established to find the optimum solution (Sokos and Zahradnik 2008):

$$\text{maximize}(m) = \text{mean}\left\{ \sum_{n=1}^{n=N} \sum_{i=1}^{i=I} \max\left[\text{cor}\left(\tilde{d}_i^m, \tilde{v}_i^n \right) \right] \right\} \quad (1)$$

Herein, $\tilde{d}_i^m$ and $\tilde{v}_i^n$ represent the energy-normalized data of the observed and modelled waveforms at the i component of sensor n, respectively; N represents the sensor number; and I denotes the number of sensor channels. Equation (1) evaluates the average over the maximum cross correlations for each sensor and component. The synthetic waveforms are aligned with the observed waveforms to obtain the maximum similarity.

Decomposition of moment tensor

The complete moment tensor m_{pq}, characterized by a second-order tensor, includes six independent elements (Aki and Richards 2002). The normalized moment tensor is used to describe the focal mechanism. The moment tensor can be decomposed into double-couple (DC), isotropic (ISO), and compensated linear vector dipole (CLVD) components. The DC component is associated with shear faulting, the ISO describes explosive or implosive sources, and the CLVD is relating to crack opening and crack closure (Vavryčuk 2001; Baig and Urbancic 2010). In our study, the percentage of each moment tensor component is calculated according to Vavryčuk (2001):

$$c^{\text{ISO}} = \frac{1}{3} \frac{\text{trace}(m)}{\max(|\lambda_i|)} \quad (2)$$

$$c^{\text{CLVD}} = 2\varepsilon(1 - |c^{\text{ISO}}|) \quad (3)$$

$$c^{\text{DC}} = 1 - \left| c^{\text{ISO}} \right| - \left| c^{\text{CLVD}} \right| \quad (4)$$

where λ_i denotes the eigenvalue of the moment tensor and ε represents the size of the CLVD relative to DC in the deviatoric moment M^{dev}, which contains non-volumetric components. The parameter ε can be expressed as

$$\varepsilon = -\frac{\lambda_{|\text{min}|}^{\text{dev}}}{\left| \lambda_{|\text{max}|}^{\text{dev}} \right|} \quad (5)$$

where $\lambda_{|\text{min}|}^{\text{dev}}$ and $\lambda_{|\text{max}|}^{\text{dev}}$ represent the minimum and maximum absolute values, respectively, of the eigenvalues of M^{dev}. For

a pure DC source, $\varepsilon = 0$, and for a pure CLVD source, $\varepsilon = \pm 0.5$. The parameter ε is positive for a tensile source and negative for a compressive source.

The slip vector u and fault normal v can be derived as (Jost and Herrmann 1989)

$$u = \frac{1}{\sqrt{2}}(t + p) \quad v = \frac{1}{\sqrt{2}}(t - p) \quad (6)$$

where t and p are the eigenvectors corresponding to the maximum and minimum eigenvalues of the moment tensor.

Global search algorithm

An inversion scheme is adopted to find out the six normalized moment tensor elements, ranging from -1 to 1 with a step size of 0.001. Differential evolution (DE) (Storn and Price 1995) is used to accelerate the search procedure and identify the moment tensor whose modelled waveforms optimally fit the observed data. The method was demonstrated by Storn and Price (1997) to be faster and can obtain greater certainty than many other global optimization methods.

The basic optimization strategy of DE is divided into four steps: initiation, mutation, crossover and selection. The initiation step generates an initial population randomly distributed over the given range. The chief difference between the DE and genetic algorithms is the mutation step, in which the mutant vector is generated as follows:

$$v_{i,G+1} = x_{r1,G} + F \times (x_{r2,G} - x_{r3,G}) \quad (7)$$

where the indexes r_1, r_2, r_3 are random integers ranging from 1 to Np, and Np is the population size. F represents the mutation factor and is a constant between 0 and 2. The crossover step increases the diversity of the population. The crossover is implemented using a binomial distribution as expressed below:

$$u_{ji,G+1} = \begin{cases} v_{ji,G+1} & \text{if } (randb(j) \leq \text{CR}) \text{ or } j = rnbr(i) \\ x_{ji,G} & \text{otherwise} \end{cases} \quad (8)$$

where i is the vector member between 1 and Np; j is the vector component between 1 and D; D is the dimension of the vector; $randb(j)$ is a random number between 0 and 1 generated for each component of the vector; CR is the crossover probability, bounded by [0 1]; and $rnbr(i)$ is randomly chosen for each vector from the interval [0 1] to ensure that $u_{ji,G+1}$ obtains at least one component from $v_{ji,G+1}$ for each population. The selection step determines the population of the next generation and is implemented through a comparison between the fitness of $u_{i,G+1}$ and $x_{i,G}$. The vector with the higher objective value is chosen to be the member of the next generation.

Velocity model and relocation

Coordinate system rotation

The Green's function is calculated in a 1-D velocity model, where the heterogeneity in the horizontal direction is ignored. As previously mentioned, the rock strata present bedding characteristics and are tilted with an attitude of N35°–55°E, SE∠15°–20°. In addition, the horizontal homogeneous assumption in the geodetic coordinate system is not consistent with the actual distribution of the rock strata in the rock slope. The error may be increased by the inaccuracies of the velocity model. Therefore, a coordinate rotation procedure is used to construct the model that reflects the rock stratum characteristics.

According to the rock strata attitude (N35°–55°E, SE∠15°–20°), the rotation procedure can be determined as follows:

1. Set the geodetic coordinate (3012895, 588904, 616) as the local-coordinate origin point;
2. Rotate the primary coordinate system by α clockwise about the U axis. We set $\alpha = 40°$ to make the N_1 axis approximately parallel to the strike of the rock strata;
3. Rotate the coordinate system counter-clockwise by β about the N_1 axis to make the E_1 axis approximately parallel with the dip of the rock strata, herein $\beta = 15°$.

Figure 4 shows the coordinate system rotation in the geodetic coordinate system. A 200 m × 310 m × 200 m cube model is established to represent the monitoring area in the new coordinate system. After rotation, the N_1–E_1

plane of the new coordinate system is roughly parallel to the rock strata. Hence, the 1-D medium model in the rotated coordinate system is in line with the horizontal homogeneous assumption and describes the medium more accurately than that in the geodetic coordinate system. According to the rock basic quality index system suggested in the Code for Hydropower Engineering Geological Investigation (GB50287-2008) issued in China, which consider the lithology of rock distributed in the left bank slope including the vertical columnar joints, the rock masses in the monitoring area can be rated as 'good' (class II) and 'fairly good' (class III_1) (see Fig. 2). The model was divided into five layers according to the distribution of different of rock masses. The suggested wave velocities of classes II and III_1 are 4700–5500 m/s and 4100–5100 m/s, respectively. The thicknesses of each layer from the top to the bottom are measured to be 44, 20, 43, 63 and 30 m, and their corresponding velocities are V_1–V_5.

Layered velocity inversion

The moment tensor inversion (MTI) can be sensitive to the velocity model. In some studies (Li et al. 2011; Song and Toksöz 2011), the layered velocity structure is derived from nearby well logs. However, the layered velocity data based on geological surveys cannot be used directly. Therefore, we retrieve the layered velocities by applying a velocity search of each layer in the given velocity range using the differences between the travel times observed and those computed for the known blast events.

The modelled travel time and the seismic ray path are calculated by resolving the eikonal equation on Cartesian domains using the multistencils fast marching methods
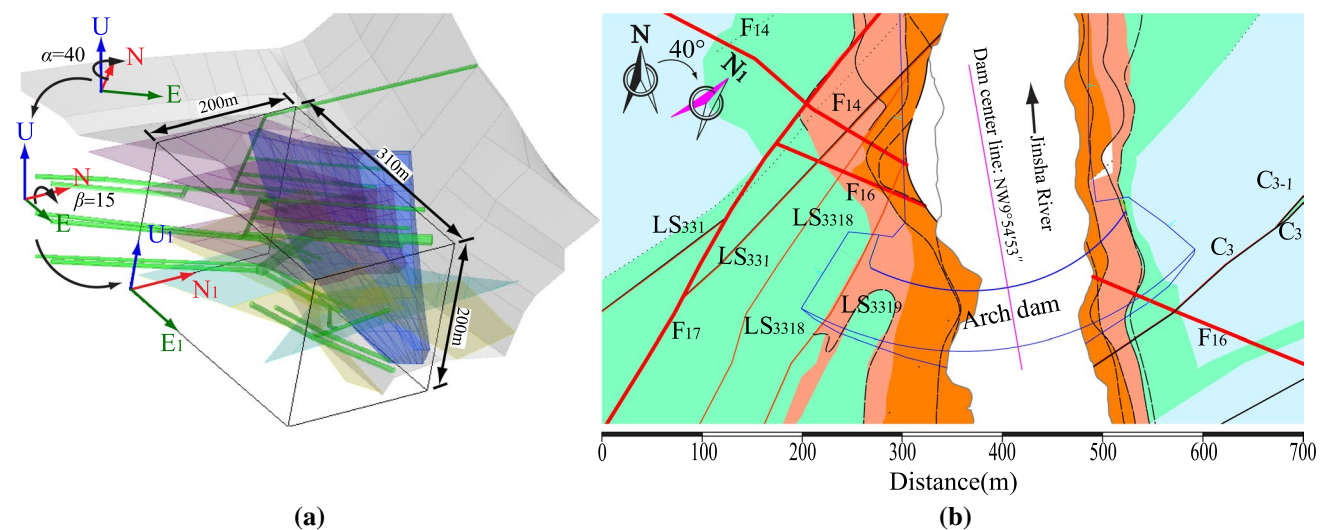

(a)   **(b)**

Fig. 4 Rotation of the coordinate system in 3D (**a**) and plane (**b**) views. The geological map in (**b**) is at the EL. 610 m, and the different colours present different types of rock mass as shown in Fig. 2

(MSFM) (Hassouna and Farag 2007). This method is an improvement of the fast marching method (FMM). According to Hassouna and Farag (2007), the second-order MSFM (MSFM$_2$) gives the highest accuracy for both isotropic and anisotropic media in both 2D and 3D models among MSFM and FMM. Moreover, this method considers the refractions and diffractions of the wave field in a very heterogeneous medium.

The same 1-D velocity model is employed to verify the ray paths of the MSFM$_2$. Figure 5 shows the ray paths between the seismic source and the receiving points calculated by the MSFM$_2$ in a 1-D model. The ray paths are bent at the interfaces of each layer, and refraction is considered during the ray path calculation of the MSFM$_2$, thereby providing a more accurate travel time than that in the homogeneous medium.

The suggested wave velocity range of each rock stratum is given based on geological surveys. The blast events involved in layered velocity inversion are listed in Table 1. The velocity search procedure, with a velocity spacing of 200 m/s, is used for each layer. The objective function is defined as the mean over the absolute value of the difference between the observed and computed travel times at the receivers. The velocities are determined to be $V_1 = 4700$ m/s, $V_2 = 4100$ m/s, $V_3 = 4700$ m/s, $V_4 = 4700$ m/s, and $V_5 = 5500$ m/s. When the objective value is minimized, the minimal value is 1.4 ms. The 1-D velocity model adopted in the present study is shown in Fig. 6.

Fig. 5 Ray paths of the MSFM$_2$ between the seismic source and receivers. **a** The 3D view of ray paths, the planes with different colours present different layer interfaces, **b** top view, **c** view to the north, and **d** view to the east. Layered velocities V_1–V_5 are randomly set, the red line presents the ray path, and different colours present different layers
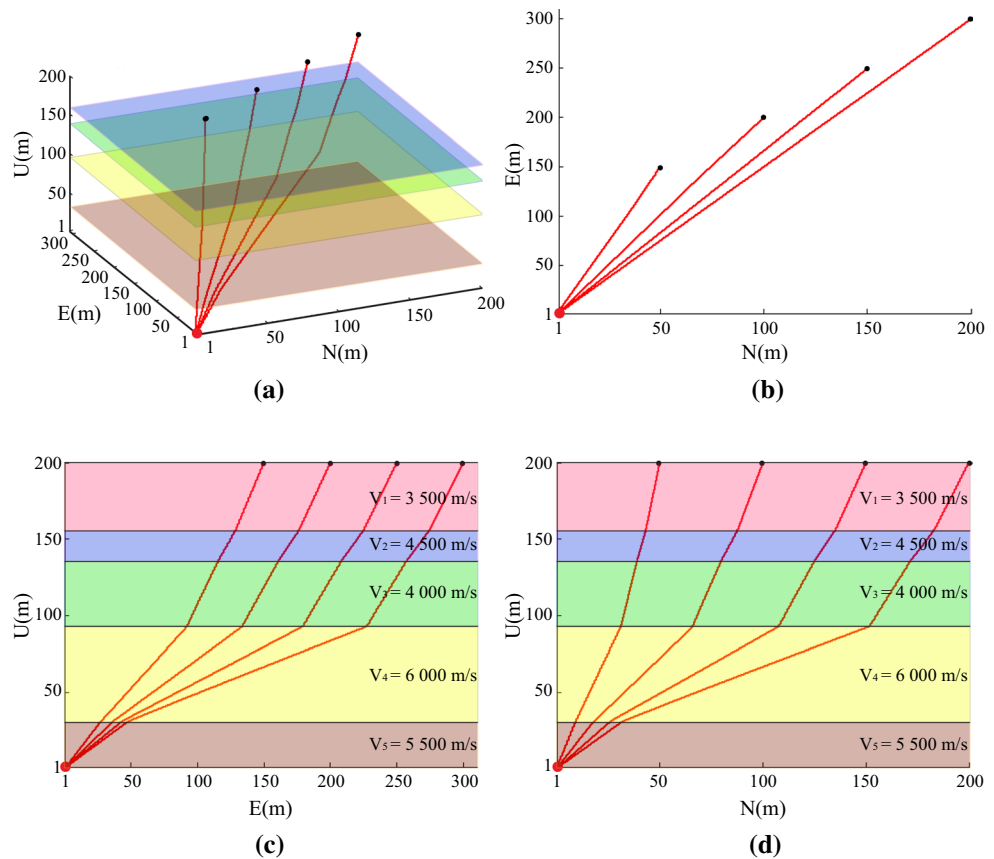

Table 1 Location of blast events used in layered velocity inversion

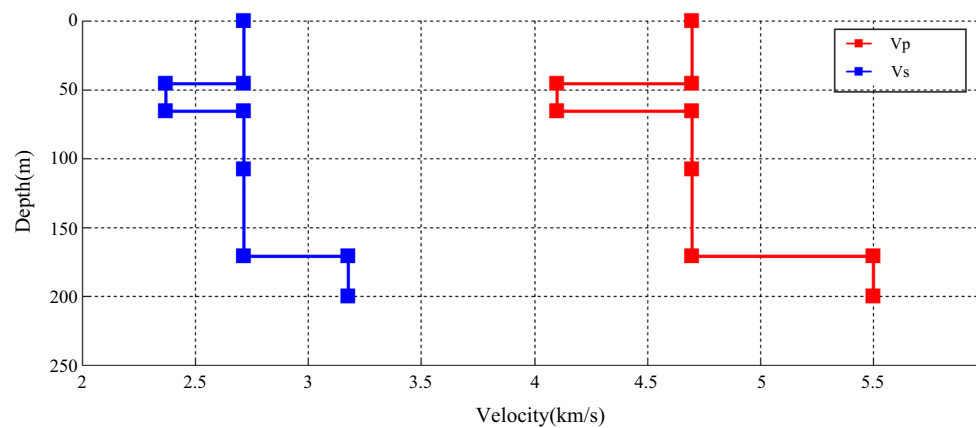| Blast events	Geodetic coordinate system			Local-coordinate system		
	N (m)	E (m)	U (m)	N' (m)	E' (m)	U' (m)
20150418152507381	3,012,794.6	589,164.1	613.3	90.3	255.5	65.7
20150419042340437	3,012,793.1	589166.7	613.0	90.8	258.4	66.1
20150418112907522	3,012,848.4	589,031.0	618.1	45.9	122.4	35.0
20150419130102706	3,012,848.4	589,028.3	617.9	44.2	120.4	34.2

Fig. 6 1-D *P*-and *S*-wave velocity model

Relocation procedure

MS event locations are traditionally determined by the MS monitoring system assuming a homogeneous rock medium model. However, due to the heterogeneity of the rock mass in the left bank slope (Fig. 2), this strategy may cause positioning errors. Since the MTI is sensitive to the MS event locations (Kühn and Vavryčuk 2013), a relocation procedure is performed in the derived 1-D velocity model (see Fig. 6) to reduce the positioning error using a homogenous medium.

The relocation is implemented by a full grid search with travel times accurately calculated by the MSFM$_2$. Based on the known velocity structure, the travel time library is efficiently calculated using the reciprocity principle, i.e., receiver stations are regarded as seismic sources. To identify the optimal location during the relocation process, the objective function of the relocation is established. This function is defined as the sum over the absolute difference between the observed and calculated travel times of the selected channels.

To validate the accuracy of the relocation procedure, the relocation of a blasting event is performed. The blast event is not involved in the layered velocity inversion step. The arrival time used in the relocation test is the same as that in the ESG location solution, which was manually picked after a certain blast event was recorded. The first 100 best solutions are used for statistical analysis, and the results are summarized in Table 2. Compared to the ESG location solution, the relocation procedure can reduce the positioning error dramatically. The results indicate that the derived velocity model (see Fig. 6) is reasonable and effective. Among the location parameters, the north direction obtains the smallest standard deviation, whereas the east obtains the largest standard deviation. The different standard deviations might be an indication of the sensitivity of the parameters.

Table 2 Results of the relocation accuracy tests

	N (m)	*E* (m)	*U* (m)	Total error (m)
Real position	3,012,791.5	589,169.4	613.0	–
ESG location	3,012,787.0	589,171.6	605.8	8.77
Relocation				
Best solution	3,012,790.4	589,170.2	611.7	1.88
Mean	3,012,790.4	589,169.6	611.3	2.03
Std.	1.40	3.60	1.53	–

The first 100 best solutions are statistically analysed to facilitate discussion of the mean and standard deviation (Std.)

Therefore, the relatively small standard deviations in Table 2 make it possible to obtain an accurate focal position.

Synthetic data validation

Synthetic data are used to validate the accuracy and robustness of the inversion procedure. The same receiver network and velocity structure are used, as shown in Figs. 3 and 6; however, only four sensors are involved in this test.

The ISOLA is used to generate clean synthetic waveforms, and a band-pass filter of 60–150 Hz is selected. The assumed source is located at the real position of the blast event involved in the relocation test, as shown in Table 2, with a pure DC focal mechanism of a strike of 200°, dip of 50°, and rake of − 30°. To consider the influence of the positioning error, the best relocation solution of the relocation test in Table 2 is used in MTI. The focal mechanism of the hypothetical source is shown in Fig. 7a.

The DE algorithm is used to find the solution that best matches the synthetic waveforms. The values of the control parameters are as follows: a population size of 100, a mutation factor of 0.5, and a crossover probability of 0.9 (Gharti et al. 2010). Figure 7b shows the focal mechanism
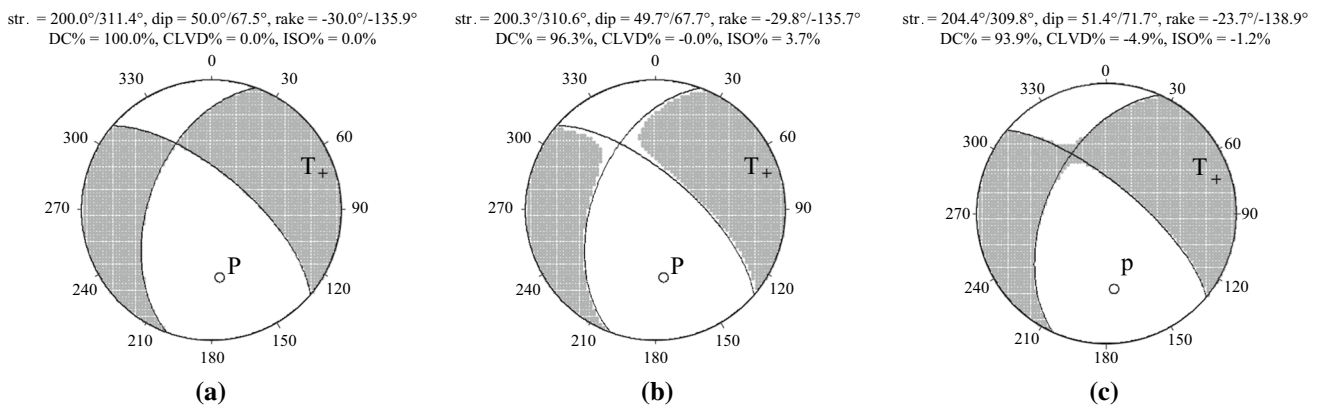
str. = 200.0°/311.4°, dip = 50.0°/67.5°, rake = -30.0°/-135.9°
DC% = 100.0%, CLVD% = 0.0%, ISO% = 0.0%

str. = 200.3°/310.6°, dip = 49.7°/67.7°, rake = -29.8°/-135.7°
DC% = 96.3%, CLVD% = -0.0%, ISO% = 3.7%

str. = 204.4°/309.8°, dip = 51.4°/71.7°, rake = -23.7°/-138.9°
DC% = 93.9%, CLVD% = -4.9%, ISO% = -1.2%

(a)   **(b)**   **(c)**

Fig. 7 Focal mechanism of the hypothetical source (**a**) and its inversion solutions. **b** The solution using the clean synthetic waveforms, **c** the solution using the noisy synthetic waveforms and the disturbed velocity model

solution determined by DE, the retrieved focal mechanism parameters are quite close to the correct solution. Among the parameters, the DC% is 96.3%, while the correct solution is 100%; additionally, the ISO% is 3.7%, while the correct solution is 0%. Nevertheless, the difference between the mechanism solution and the correct solution has little influence on understanding the seismic source.

Figure 8 shows the optimization process. The objective function value increases quickly in the preliminary stage of the optimization but later becomes relatively slow. After a certain number of generations, the fault-plane solution of the DC component remains consistent with the correct solution, and the DC% approximates the correct value with increasing generation number.

The inversion procedure is further validated by adding noise to the clean synthetic seismograms and by disturbing the velocity model (see Fig. 6) to simulate the noise contamination and the inaccuracy of the velocity model in the field data. White Gaussian noise is added to each trace. The noise level is estimated through the signal-to-noise ratio

(SNR), which is 0.001 dB after contamination. The noisy synthetic waveforms are filtered in a frequency range of 60–150 Hz, as is done for the real field data. The disturbance of both *P*- and *S*-wave velocity models is implemented by adding 5% of the original velocity for each layer, and the disturbance is independent for *P*- and *S*-waves. The density and thickness of each layer remain constant during the test because the density and depth of each rock stratum are measured based on the geological survey, and the velocity error is dominant in determining the characteristics of the modelled waveforms (Li et al. 2011). The disturbed velocity model is shown in Fig. 9.

Figure 7c shows the focal mechanism solution using the noisy synthetic waveforms and the disturbed velocity model. The control parameters in DE are the same as those used above. The values are close to the correct solutions. However, compared to clean synthetic waveforms, the difference between the inversion focal mechanism and the correct solution increases due to the noise contamination and model disturbances.
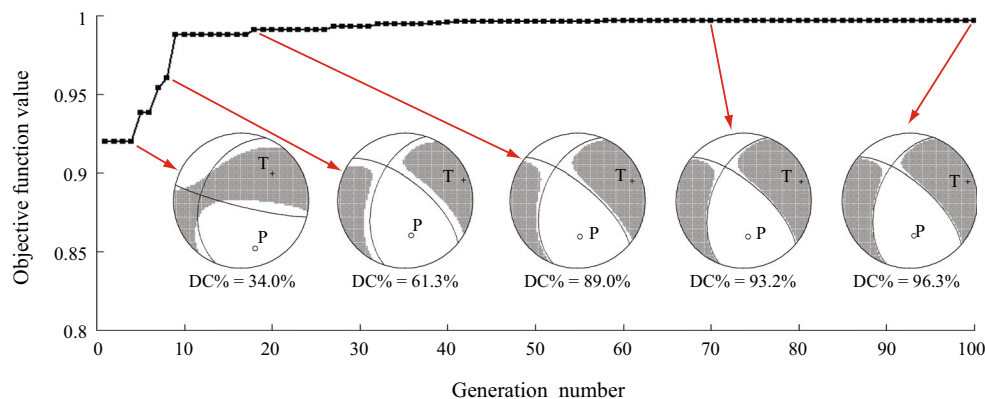
Fig. 8 Convergence process of the objective function during the optimization of DE

Figure 10 compares the modelled waveforms and the synthetic waveforms. The level of similarities between these two types of waveforms is quite high, which may be attributed to the filtering process applied to both the modelled and synthetic data.

A statistical analysis is further performed on the distribution of the focal mechanical parameters from the first 100 best solutions during the optimization process. The results are listed in Table 3. The mean value of the parameters is close to the correct solution. Among the standard deviations, the DC, CLVD, VOL parameters obtain larger standard deviations than those of the strike, dip, and rake. However, their values are quite small, revealing that the matching process is thoroughly optimized.

Moment tensor inversion of MS events

Rotation of the seismograms

Different as the tests on the synthetic data, the directions of the modelled seismograms and the observed data are not consistent because of the sensor installation orientation (see Fig. 3). To eliminate the influence of the sensor installation orientation on the received seismic signal and to ensure that the modelled waveform matches the recorded waveform, a seismogram rotation procedure is implemented for the modelled waveforms in the new coordinate system prior to matching.

For a three-component seismogram, the waveforms can be rotated into a new orientation system by a rotation

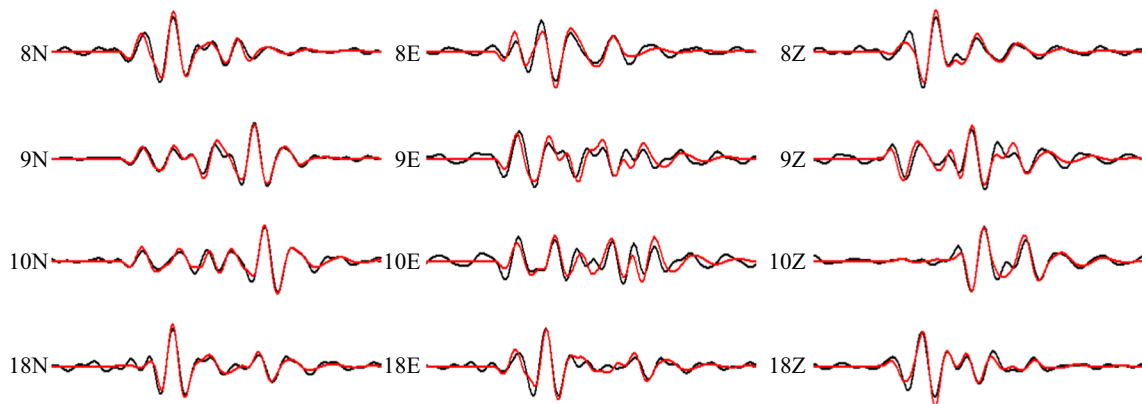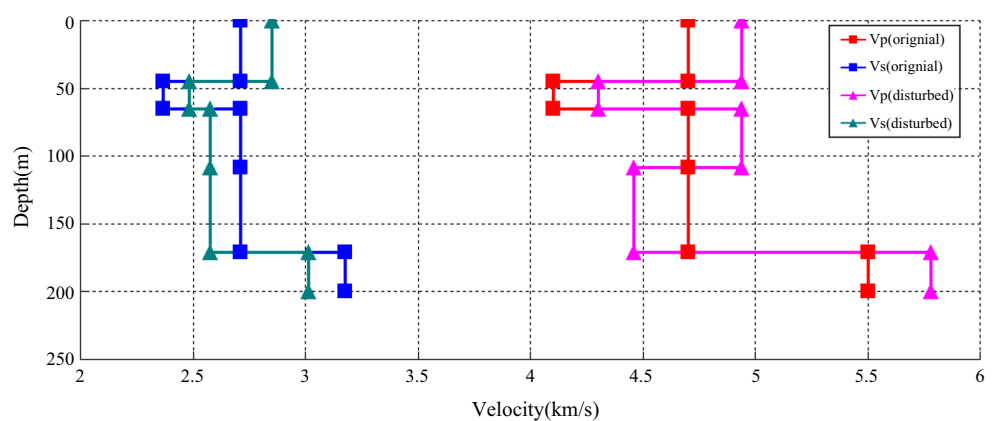**Fig. 9** Disturbed and original velocity model

Fig. 10 Comparison between the synthetic (black) and modelled (red) waveforms. The synthetic waveforms used to match are contaminated by white Gaussian noise and the modelled waveforms are generated by the disturbed velocity model

Table 3 Statistics of the first 100 best solutions of synthetic data

	DC (%)	CLVD (%)	VOL (%)	Strike (°)	Dip (°)	Rake (°)
Mean	94.1	− 4.5	− 1.3	204.6/309.7	51.7/71.7	− 23.5/− 139.3
Std.	1.5	1.1	1.1	0.3/0.2	0.4/0.3	0.5/0.4

The results are calculated using the noisy synthetic waveforms and the disturbed velocity model

matrix (Wamboldt 2012). The transform procedure can be expressed as

$$
\left\{
\begin{array}{ccccc}
u_{1'1} & u_{1'2} & u_{1'3} & \ldots & u_{1'n} \\
u_{2'1} & u_{2'2} & u_{2'3} & \ldots & u_{2'n} \\
u_{3'1} & u_{3'1} & u_{3'1} & \ldots & u_{3'n}
\end{array}
\right\}
= \text{ROT}_{3\times3}
\left\{
\begin{array}{ccccc}
u_{11} & u_{12} & u_{13} & \ldots & u_{1n} \\
u_{21} & u_{22} & u_{23} & \ldots & u_{2n} \\
u_{31} & u_{31} & u_{31} & \ldots & u_{3n}
\end{array}
\right\}
\tag{9}
$$

where u_{ij} is the jth point of the ith channel in the seismogram time series and $\text{ROT}_{3\times3}$ is the 3×3 rotation matrix, which is determined by Eq. 10.

$$
\text{TO}'_{3\times3} = \text{ROT}_{3\times3} \times \text{TO}_{3\times3}
\tag{10}
$$

where $\text{TO}_{3\times3}$ and $\text{TO}'_{3\times3}$ are the original and rotated orientation matrices, respectively. The 3×3 orientation matrix describes the relative orientation of the orthogonal components for each sensor. The original orientation matrix $\text{TO}_{3\times3}$ is determined by the modelled seismograms. In ISOLA, the $\text{TO}_{3\times3} = E_3$, and the rotated orientation matrix $\text{TO}'_{3\times3}$ is determined by the orientation of the corresponding sensors; its value is

$$
\text{TO}'_{3\times3} =
\begin{bmatrix}
\cos\theta_{11} & \cos\theta_{12} & \cos\theta_{13} \\
\cos\theta_{21} & \cos\theta_{22} & \cos\theta_{23} \\
\cos\theta_{31} & \cos\theta_{32} & \cos\theta_{33}
\end{bmatrix}
\tag{11}
$$

where θ_{ij} is the angle between the ith component of sensor and jth component of coordinates. Inserting (11) into (10), the rotation matrix $\text{ROT}_{3\times3}$ can be expressed as

$$
\text{ROT}_{3\times3} = \text{TO}'_{3\times3} =
\begin{bmatrix}
\cos\theta_{11} & \cos\theta_{12} & \cos\theta_{13} \\
\cos\theta_{21} & \cos\theta_{22} & \cos\theta_{23} \\
\cos\theta_{31} & \cos\theta_{32} & \cos\theta_{33}
\end{bmatrix}
\tag{12}
$$

Using the seismogram rotation procedure, the modelled waveform is able to match the recorded data.

Moment tensor inversion of MS data

Before MTI, an essential step is to select suitable MS events for inversion. The following selection criterion is adopted: MS events are recorded using at least 6 sensors and with a high SNR. Finally, we arrived at 12 MS events, and their positions are listed in Table 4.

First, the analysis procedure for a typical MS event is described herein. Figure 11 shows the waveforms and their spectrograms of the MS event 20151109151107914 recorded by the sensors involved in MTI. The optimization control parameters used for the MS data are the same as those used for the synthetic data test. Similar to the synthetic data test, the first 100 best solutions during the optimization process are selected to evaluate the statistics of the focal mechanism parameters. The statistical results are tabulated in Table 5.

Table 4 Relocation of the selected MS events

No.	MS events	N (m)	E (m)	U (m)
1	20151104041544028	3,012,881.7	589,103.4	742.6
2	20151108210709578	3,012,844.4	589,028.1	713.3
3	20151108210749278	3,012,912.4	589,082.4	736.6
4	20151109151107914	3,012,841.0	589,024.4	738.3
5	20151110182106066	3,012,839.3	589,096.4	704.6
6	20151111035825323	3,012,897.5	589,109.5	753.3
7	20151114230919624	3,012,904.6	589,115.1	748.3
8	20151121183113933	3,012,860.0	589,127.8	725.5
9	20151121184415126	3,012,812.9	589,155.9	706.5
10	20160121120852845	3,012,835.4	589,131.7	649.6
11	20160122065116840	3,012,815.2	589,133.7	630.2
12	20160127161216804	3,012,848.9	589,092.6	663.0

The first 100 best solutions are highly centralized, and the standard deviations of the parameters are extremely small, indicating that the optimization procedure is highly robust.

Figure 12 compares the recorded data and the modelled data. A good agreement can be observed between the dominant modelled and observed waveforms. The unmatched waveform parts are most likely due to the random noise contamination and the errors of the location and medium model.

Table 6 shows the mechanism solutions of the selected MS events in Table 4. The standard deviations of the first 100 best solutions of each parameter are used to evaluate the optimization process. Among them, the smallest standard deviation is 0.03, while the largest is 3.9. The small standard deviation values in Table 6 indicate that the matching process is completely optimized. Concerning the DC component, which is important for understanding the fracture process experienced by the rock mass, the maximum DC percentage is 84.81%, and the minimum is 8.51%. Overall, 2 out of 12 MS events have a DC% of greater than 50%, which indicates that the selected MS events occurring in the rock slope are characterized by significant non-shear focal mechanisms. According to the above-mentioned construction schedule, the excavation of the left bank slope was suspended from January 2015 to February 2016, and construction activities were mainly concentrated on the excavation of various tunnels in the rock slope and on supporting and consolidation grouting of the rock slope. The supporting and grouting works during the suspended period might play a large role in controlling the potential sliding of the rock slope, resulting in the relatively low DC%. The grouting with high-pressure liquid cement may cause pre-existing cracks to open, resulting in the occurrence of MS events with predominant non-DC components and positive volumetric components. Similar phenomenon was also detected by Šílený et al. (2009) in hydraulic fracturing. The roof and sidewalls of
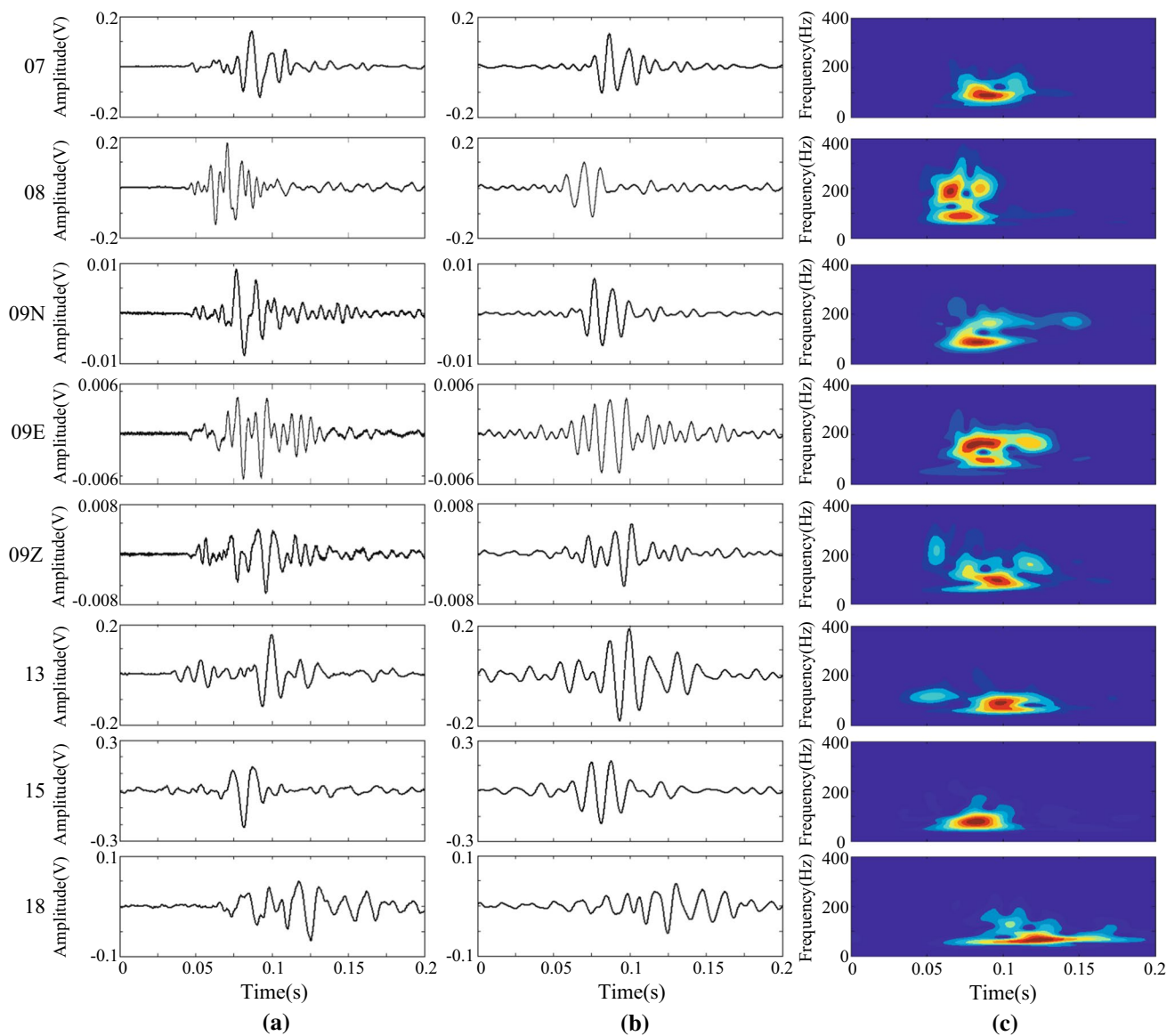
Fig. 11 Waveforms and their corresponding spectrograms of MS event 20151109151107914 recorded by the selected sensors involved in MTI. **a** The original seismograms, **b** the filtered seismograms (60–150 Hz), and **c** the spectrograms of the original seismograms obtained through S transform (Stockwell et al. 1996)

Table 5 Statistics of the first 100 best solutions during the optimization process of MS event 20151109151107914

	DC (%)	CLVD (%)	VOL (%)	Strike (°)	Dip (°)	Rake (°)
Best	36.6	− 32.4	− 31.1	30.6/300.4	87.8/84.9	5.2/177.7
Mean	37.0	− 32.1	− 31.0	30.6/300.4	87.9/84.9	5.1/177.9
Std.	0.92	0.76	0.31	0.03/0.05	0.42/0.42	0.42/0.42

tunnels in the rock slope might collapse due to excavation-induced unloading, which will result in the occurrence of MS events with a significant non-shear focal mechanism (Kühn and Vavryčuk 2013), especially for the regions of columnar jointed basalts in the slope (Jiang et al. 2014; see Fig. 2).

Figure 13 shows the positions of the selected MS events and the orientations of the DC components. As shown in Fig. 13, a majority of the MS events have an approximate N–S direction fault-plane solution, agreeing with the strike of the rock strata (Fig. 4). This suggests that the MTI is successful. Concerning the 2 relatively high DC% (> 50%)
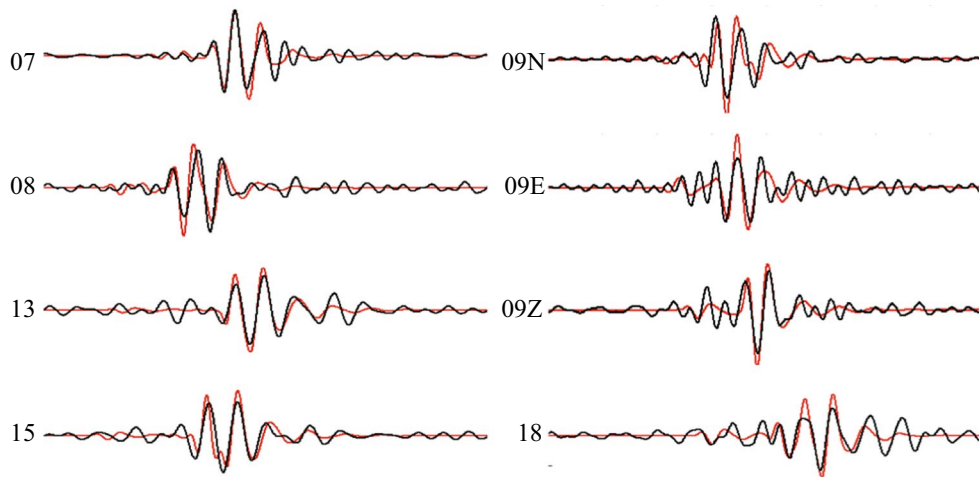
Fig. 12 Comparison between the modelled (red) and recorded (black) waveforms of MS event 20151109151107914 at the selected sensors

Table 6 Focal mechanisms of the selected MS events and standard deviations of the first 100 best solutions during the optimization process

Event	DC (%) Best/Std.	CLVD (%) Best/Std.	ISO (%) Best/Std.
1	34.3/1.3	38.7/1.1	27.1/0.6
2	31.5/0.8	28.7/1.0	39.8/1.1
3	69.4/3.0	− 8.8/2.5	− 21.8/1.5
4	36.6/0.9	− 32.4/0.8	− 31.1/0.3
5	84.8/0.1	− 0.5/1.0	− 14.7/0.9
6	44.9/0.5	− 1.7/0.8	− 53.4/0.4
7	34.6/0.5	− 12.3/0.4	− 53.2/0.3
8	8.5/1.4	− 33.2/1.2	− 58.3/0.8
9	28.4/1.5	− 6.3/0.9	65.4/0.8
10	48.4/0.7	− 9.7/0.8	− 41.9/0.5
11	41.6/2.9	23.5/3.9	34.9/3.4
12	24.2/0.3	14.9/0.3	60.9/0.2

| Event	Strike(°) Best/Std.		Dip (°) Best/Std.		Rake (°) Best/Std.	
1	31.1/1.5	295.5/1.5	78.3/0.7	64.9/1.0	25.7/1.0	167.0/0.7
2	197.3/1.0	289.5/1.0	89.1/0.5	21.6/1.3	− 68.4/1.3	− 177.6/0.5
3	158.5/0.4	250.6/0.2	85.8/0.4	64.1/0.7	− 26.0/0.7	− 175.3/0.4
4	30.6/0.03	300.4/0.05	87.8/0.4	84.9/0.4	5.2/0.4	177.7/0.4
5	180.9/0.1	327.7/0.6	83.4/0.1	7.9/0.1	94.3/0.1	57.0/0.6
6	334.3/0.6	105.4/0.4	21.7/0.3	75.3/0.2	136.8/0.7	73.8/0.4
7	6.4/0.2	275.8/0.2	71.2/0.2	88.5/0.2	− 178.4/0.4	− 18.8/ 0.4
8	198.3/2.2	72.1/1.7	62.8/0.9	41.1/2.4	58.0/3.2	135.9/2.7
9	189.1/1.4	12.4/1.8	47.2/0.4	42.8/0.5	− 92.3/0.7	− 87.5/0.7
10	17.5/0.4	144.5/0.3	30.9/0.2	70.2/0.3	− 41.4/0.6	− 114.2/0.3
11	16.9/1.0	112.7/0.6	69.6/2.4	74.7/1.2	163.7/1.2	21.2/2.4
12	28.8/1.6	205.9/0.3	11.5/0.2	78.6/0.2	92.8/1.5	89.4/0.3
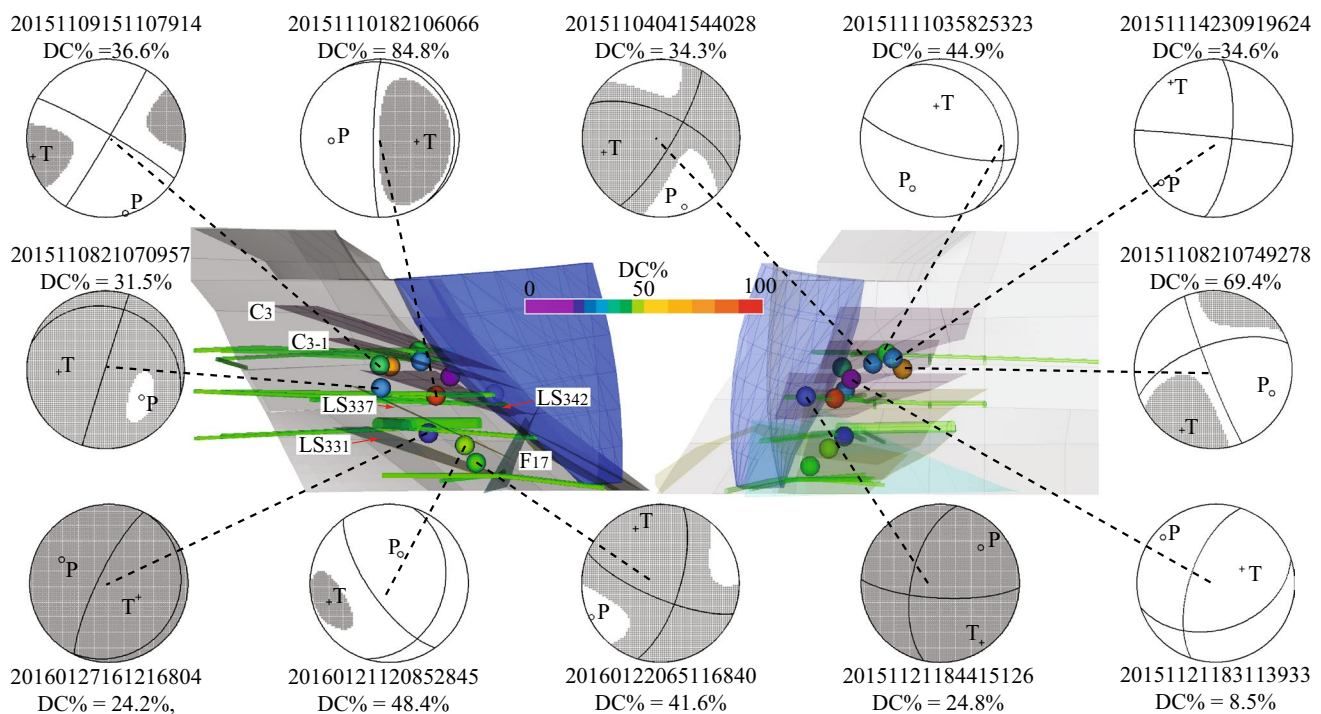
Fig. 13 Mechanisms of the selected MS data. The two central pictures are the position of the MS events under different views. The colour of the sphere presents the DC% of the corresponding MS event; the brighter the colour, the higher the DC%

MS events in Table 6, both of them are located near LS$_{342}$. This suggests that LS$_{342}$ may represent the potential sliding surface of the slope, which might cause slope instability during later excavation.

Conclusions

The determination of the focal mechanism of MS events occurring in rock engineering is important for hazard evaluation and forecasting. The waveform matching method was used to determine the moment tensor of the MS events recorded in the left bank slope of the Baihetan hydropower station. The ISOLA code was employed to generate the modelled waveforms for a certain focal mechanism. The DE optimization algorithm was used to find out the focal mechanism solution and its corresponding modelled waveforms that best match the observed data recorded by an MS monitoring system. The following conclusions can be drawn.

1. To obtain an accurate 1-D velocity model, the coordinate system is rotated to agree with the attitude of the rock strata, and the velocity structure is obtained through velocity inversion based on geological survey results and known blasts. A relocation procedure is adopted to obtain an accurate source location. The relocation testing shows that the proposed relocation method can

improve the positioning error dramatically and that the derived 1-D velocity model used is reasonable.

2. A synthetic data test is adopted to test the robustness of the inversion procedure. The results show that this method is robust and can provide accurate solutions when subject to positioning errors, noise contamination and velocity model disturbances. The small standard deviations of the first 100 solutions during the optimization process indicate that the matching process is fully optimized.

3. For the field-monitored data, the predominant non-DC components are detected in the rock slope, which may be attributed to the collapse due to excavation, consolidation grouting and supporting of the rock slope. A majority of the selected MS events have a strike consistent with that of rock strata under the rotated coordinate system, which proves that the moment tensor inversion is reliable. The position analysis of the relatively high DC events suggests that LS$_{342}$ is the potential sliding surfaces of the rock slope, and greater attention should be paid to this area during later excavation.

and Geoenvironment Protection (Chengdu University of Technology) (No. SKLGP2016K018).

References

Aki K, Richards PG (2002) Quantitative seismology. University Science Books, Sausalito

Baig A, Urbancic T (2010) Microseismic moment tensors: a path to understanding frac growth. Lead Edge 29(3):320–324

Bouchon M (1981) A simple method to calculate Green's function for elastic layered media. Bull Seism Soc Am 71(4):959–971

Bouchon M (2003) A review of the discrete wavenumber method. Pure Appl Geophys 160(3–4):445–3465

Carvalho J, Barros LV, Zahradík J (2015) Focal mechanisms and moment magnitudes of micro-earthquakes in central Brazil by waveform inversion with quality assessment and inference of the local stress field. J S Am Earth Sci. https://doi.org/10.1016/j.jsames.2015.07.020

Dai F, Li B, Xu NW, Meng G, Wu J, Fan YL (2017) Microseismic monitoring of the left bank slope at the Baihetan hydropower station, China. Rock Mech Rock Eng 50(1):225–232

Gharti HN, Oye V, Roth M, Kühn D, Roth M (2010) Automated micro-earthquake location using envelope stacking and robust global optimization. Geophysics 75(4):27–46

Hassouna MS, Farag AA (2007) Multistencils fast marching methods: a highly accurate solution to the eikonal equation on Cartesian domains. IEEE Trans Pattern Anal Mach Intell 29(9):1563–1574

Jiang Q, Feng XT, Hatzor YH, Hao XJ, Li SJ (2014) Mechanical anisotropy of columnar jointed basalts: an example from the Baihetan hydropower station, China. Eng Geol 175:35–45

Jost ML, Herrmann RB (1989) A student's guide to and review of moment tensors. Seismol Res Lett 60(2):37–57

Köhn D, De Nil D, Hagrey SA, Al Rabbel W (2016) A combination of waveform inversion and reverse-time modelling for microseismic event characterization in complex salt structures. Environ Earth Sci 75(18):1235

Kühn D, Vavryčuk V (2013) Determination of full moment tensor of microseismic events in a very heterogeneous mining environment. Tectonophysics 589:33–43

Li JL, Zhang HJ, Kuleli HS (2011) Focal mechanism determination using high-frequency waveform matching and its application to small magnitude induced earthquakes. Geophys J Int 184(3):1261–1274

Liu JP, Feng XT, Li YH, Xu SD, Sheng Y (2013) Studies on temporal and spatial variation of microseismic activities in a deep metal mine. Int J Rock Mech Min Sci 60:171–179

Lu CP, Liu GJ, Liu Y, Zhang N, Xue JH, Zhang L (2015) Microseismic multi-parameter characteristics of rockburst hazard induced by hard roof fall and high stress concentration. Int J Rock Mech Min Sci 76:18–32

Šílený J, Milev A (2006) Seismic moment tensor resolution on a local scale: simulated rockburst and mine-induced seismic events in the Kopanang gold mine, South Africa. Pure Appl Geophys 163(8):1495–1513

Šílený J, Hill DP, Eisner L, Cornet FH (2009) Non-double-couple mechanisms of microearthquakes induced by hydraulic fracturing. J Geophys Res. https://doi.org/10.1029/2008JB005987

Sokos EN, Zahradnik J (2008) ISOLA a Fortran code and a Matlab GUI to perform multiple-point source inversion of seismic data. Comput Geosci 34(8):967–977

Song FX, Toksöz MN (2011) Full-waveform based complete moment tensor inversion and source parameter estimation form downhole microseismic data for hydrofracture monitoring. Geophysics 76(6):103–116

Stockwell RG, Mansinha L, Lowe R (1996) Localization of the complex spectrum: the S transform. IEEE Trans Signal Process 44(4):998–1001

Storn R, Price K (1995) Differential evolution: a simple and efficient adaptive scheme for global optimization over continuous spaces. Berkeley: Tech Rep TR-95-012 ICSI

Storn R, Price K (1997) Differential evolution—a simple and efficient heuristic for global optimization over continuous spaces. J Glob Optim 11(4):341–359

Tang LZ, Xia KW (2010) Seismological method for prediction of areal rockbursts in deep mine with seismic source mechanism and unstable failure theory. J Cent South Univ Technol 17(5):947–953

Vavryčuk V (2001) Inversion for parameters of tensile earthquakes. J Geophys Res 106(B8):16339–16355

Vavryčuk V (2007) On the retrieval of moment tensors from borehole data. Geophys Prospect 55(3):381–391

Vavryčuk V, Kühn D (2012) Moment tensor inversion of waveforms: a two-step time-frequency approach. Geophys J Int 190(3):1761–1776

Wamboldt L (2012) An automated approach for the determination of the seismic moment tensor in mining environments. M.S. Thesis. Queen's University, Kingston, Ontario, Canada

Xiao YX, Feng XT, Feng GL, Liu HJ, Jiang Q, Qiu SL (2016) Mechanism of evolution of stress–structure controlled collapse of surrounding rock in caverns: a case study from the Baihetan hydropower station in China. Tunn Undergr Sp Technol 51:56–67

Xu NW, Tang CA, Li LC, Zhou Z, Sha C, Liang ZZ, Yang JY (2011) Microseismic monitoring and stability analysis of the left bank slope in Jinping first stage hydropower station in southwestern China. Int J Rock Mech Min Sci 48(6):950–963

Xu NW, Dai F, Liang ZZ, Zhou Z, Sha C, Tang CA (2014) The dynamic evaluation of rock slope stability considering the effects of microseismic damage. Rock Mech Rock Eng 47(2):621–642

Xu NW, Li TB, Dai F, Li B, Zhu YG, Yang DS (2015) Microseismic monitoring and stability evaluation for the large scale underground caverns at the Houziyan hydropower station in Southwest China. Eng Geol 188:48–67

Xu NW, Li TB, Dai F, Zhang R, Tang CA, Tang LX (2016a) Microseismic monitoring of strainburst activities in deep tunnels at the Jinping II hydropower station, China. Rock Mech Rock Eng 49:981–1000

Xu NW, Dai F, Zhou Z, Jiang P, Zhao T (2016b) Microseismicity and its time–frequency characteristics of the left bank slope at the Jinping first-stage hydropower station during reservoir impoundment. Environ Earth Sci 75(7):608. https://doi.org/10.1007/s12665-016-5539-z

Zhang J, Zhang HJ, Chen EH, Zheng Y, Kuang WH, Zhang X (2014) Real-time earthquake monitoring using a search engine method. Nat Commun. https://doi.org/10.1038/ncomms6664